Materials Science & Engineering A 700 (2017) 583–591

Contents lists available at ScienceDirect

Materials Science & Engineering A

journal homepage: www.elsevier.com/locate/msea

Degradation and onset of plastic anisotropy in marine aluminum alloy due to fire exposure by bulk neutron diffraction and in situ loading

Stephen B. Puplampu[a], Dayakar Penumadu[a,*], Ran Ma[a], Timothy J. Truster[a], Robin Woracek[b], E. Andrew Payzant[c], Jeffrey R. Bunn[c]

[a] The University of Tennessee Knoxville, TN 37996-2313, USA
[b] European Spallation Source ESS ERIC, SE-221 00 Lund, Sweden
[c] Oak Ridge National Lab, Oak Ridge, TN 37892, USA

ARTICLE INFO

Keywords:
Neutron scattering
Strain measurement
Polycrystal
Aluminum alloys
Mechanical properties
Crystal plasticity

ABSTRACT

In this paper, the degradation of mechanical properties of marine structural aluminum alloy AA5083 and onset of lattice plastic anisotropy subsequent to fire exposure is investigated. For virgin and fire-exposed samples, microstructural characterization is carried out for the first time and changes in lattice specific strain responses under step and continuous axial deformation are studied using novel bulk neutron diffraction. Peak fitting of raw data yields d-spacing values of reflections of interest and allows for lattice specific strain calculations. A reduction in yield stress from 260 MPa in the virgin material to 120 MPa in the fire-exposed sample is observed. Virgin material exhibits dynamic strain aging during plastic deformation; this is captured in neutron diffraction measurements. Larger peak broadening for virgin material indicates possible presence of Type II and III residual stresses due to intergranular stress or dislocation stress fields. Stress vs. lattice strain plots show large deviations from linearity post-yield for fire-exposed samples. This is due to strain redistribution among grains as well as grain reorientation. After fire exposure dynamic strain aging does not occur, but individual lattice planes reveal plastic anisotropy in their response to plastic deformation. Results from neutron diffraction, combined with electron backscatter diffraction characterization, provide insight into the yielding mechanisms of AA5083 and effects of fire exposure.

1. Introduction

1.1. Background

The material studied herein is an aluminum alloy, AA5083, of interest to the US Navy for use in naval structures. Compared to other alloys such as the AA6061 alloy (also used for naval structural purposes), AA5083 contains a higher percentage of magnesium and is known for its resistance to corrosion in harsh environments such as seawater [1,2]. AA5083 is a solid solution strengthened alloy and generally displays good weldability and retains strength and toughness properties of parent material [3–5]. Introduction of Magnesium, as is the case with other aluminum alloys of the 5000 series, vastly improves mechanical properties and yield stress of pure aluminum [6]. The main alloying elements of AA5083 aluminum are Magnesium and Manganese; detailed chemical composition is shown in Table 1 [7]:

Structural materials in naval vessels are subjected to complex thermo-mechanical processes (high temperatures, multi-axial loading involving rotation of principal stresses). Several processing factors involved with the manufacturing and machining of these alloys such as rolling procedure and machining/joining conditions play an important role in how the material responds to loading conditions and fire exposure. Past studies on AA5083 examined the effects of heat sensitization on corrosion resistance and mechanical properties. For these tests, samples were subjected to temperatures ranging from 100 °C to 200 °C. Data was acquired by a variety of methods including scanning electron microscopy (SEM), energy dispersive X-ray spectroscopy (EDS) and hardness measurements, finding that reduction in strength and hardness was due to recrystallization and decrease in concentration of Mg atoms [8]. Similar studies looked at the effects of strain rate and constituent particle size at elevated temperature in AA5083 [9] as well as corrosion-fatigue behavior [10]. Samples were loaded in tension to desired stress and then quenched. Microstructure evolution was assessed by electron backscattter diffraction (EBSD) for grain size and texture. Authors found recrystallized grains had random texture while grains that had not undergone recrystallization presented strong

* Corresponding author.
E-mail address: dpenumad@utk.edu (D. Penumadu).

http://dx.doi.org/10.1016/j.msea.2017.06.050
Received 9 January 2017; Received in revised form 11 June 2017; Accepted 12 June 2017
Available online 13 June 2017
0921-5093/

Table 1
Chemical composition of aluminum alloy AA5083.

Component	Weight %
Al	92.4–95.6
Mg	4.0–4.9
Si	< 0.40
Cr	0.05–0.25
Mn	0.40–1.0
Ti	Max 0.15
Cu	Max 0.10
Zn	Max 0.25
Fe	Max 0.40
Other	Max 0.15

texture. Others investigated residual properties as influenced by heating rate and final temperature. Residual mechanical properties were measured during uniaxial tension tests by strain gages and 3D imaging correlation. Similarly, property degradation was attributed to grain recrystallization and removal of dislocations [11]. Fire exposure in ship structures is an important consideration and thermal effects associated with fire exposure and subsequent fire suppression agents lead to degradation of its mechanical properties. When inspecting mechanical properties of textured materials, specific crystallographic lattice plane response to applied loads can reveal crystal anisotropy leading to preferred failure modes [12]. While x-ray diffraction is a preferred method for surface measurements of lattice strains, neutron diffraction is very effective for evaluating the strain in the bulk of the sample due to the ability of neutron radiation to have high penetration of common structural alloys. Neutron diffraction has been used extensively to probe materials' atomic planar spacing (d-spacing) changes for various crystallographic planes under applied loadings [12–15]. For example, the lattice strain response has been investigated for tensile loading of annealed aluminum 2% magnesium alloy showing an isotropic response in the elastic region [16].

In the present study, the effect of fire (simulated by high-temperature exposure and subsequent quenching) on the mechanical properties of the aluminum 5083 alloy (4–4.9% magnesium) was probed by in-situ bulk neutron diffraction under continuous tensile loading. For these experiments, thermal neutrons were used. In general, the thermal neutron source is typically a reactor (as opposed to a spallation source for pulsed neutrons) which provides a continuous, high flux, beam of neutrons with a wavelength of choice (desired wavelength is selected by way of a tunable monochromator). Using thermal neutrons generally allows probing only a single reflection at a given time but on the other hand due to the high flux available acquisition times are greatly reduced and materials can be subjected to dynamic, time-dependent tests. For a more comprehensive study, mechanical tests were repeated using different instrument parameters to investigate behavior of additional reflections. Virgin material and fire-exposed samples were subjected to a series of uni-axial deformation tests employing step loading to determine lattice specific elastic moduli and then, as a novel procedure, continuous axial deformation tests beyond elasticity into the plastic region of the stress-strain curve. The purpose is to characterize lattice strain response and associated differences due to fire damage. After mechanical testing, texture and microstructural changes were assessed ex-situ by EBSD and EDS. Data presented in this paper is used to develop a crystal plasticity finite element based model accounting for grain orientation and texture to consider meso-scale effects [17].

1.2. Theory

In neutron diffraction measurements, lattice strain information is obtained from Bragg's law:

$$2d \sin\theta = \lambda, \tag{1}$$

The diffraction instrument generates a monochromatic neutron beam with wavelength $\boldsymbol{\lambda}$ which, upon interaction with the polycrystalline material under study, diffracts by specific scattering angles $\boldsymbol{\theta}$ based on material properties, in particular the spacing of lattice planes $\boldsymbol{d}$.

Reference d-spacings for *hkl*'s of interest, d^0_{hkl}, will be measured at a seating tensile load which effectively will act as a "zero load" reference. With increasing loads d-spacing changes are progressively measured. Lattice strain, $\varepsilon_{(hkl)}$, can then be computed from Eq. (2):

For a reference spacing for a given plane d^0_{hkl} corresponding to initial state prior to application of external loading; lattice strain, $\varepsilon_{(hkl)}$, and lattice specific moduli, $E_{(hkl)}$, are obtained based on Eqs. (2) and (3) respectively:

$$\varepsilon_{hkl} = \frac{d_{hkl} - d^0_{hkl}}{d^0_{hkl}} \tag{2}$$

From the linear portion of the stress-strain curve a lattice specific modulus can be obtained:

$$E_{hkl} = \frac{\sigma}{\varepsilon_{hkl}} \tag{3}$$

2. Experimental method

2.1. Overview

For the reported measurements in this paper, *hkl*'s of interest were (311), (222) and (400). Behavior for these reflections has been investigated in the past, for a different aluminum alloy, to determine how they are influenced by intergranular strains [14]. Probing the mechanical properties of structural alloys beyond elasticity into the plastic region by using time of flight neutron diffraction, step loading was employed for a magnesium alloy [15]. In the present research, tests were conducted using a high flux thermal neutron source allowing d-spacing measurements semi-continuously for insight into the dynamic evolution of the material's microstructure; authors' interest was in the comparison of the yield process between virgin material samples and fire-exposed samples. During neutron diffraction measurements testing was carried out using a custom developed portable mechanical loading system, capable of applying tensile (up to 22 kN) and torsional (up to 112 N m) loads [18,19]; the macroscopic stress-strain behavior, including plastic deformation, was monitored subsequently during separate tests using VIC-3D™, a digital image correlation (DIC) system for on specimen strain mapping [20]. Macroscopic Young's modulus E was calculated from the linear fit of the elastic region of the stress-strain curve and yield stress σ_Y was determined using a 0.2% offset of elastic response.

2.2. Sample description

Dog-bone shaped samples were obtained from AA5083 plates; all samples were machined along the rolling direction. The sample dimensions are shown in Fig. 1(a). Four samples were conditioned at 400 °C for 30 min in a furnace and then water-quenched to simulate effects of fire damage and fire suppression agents.

2.3. Instrument description

Authors carried out measurements at the Neutron Residual Stress Mapping Facility (NRSF2) located at the HB-2B thermal port of the High Flux Isotope Reactor (HFIR) at the Oak Ridge National Laboratory (ORNL). NRSF2 makes use of a tunable monochromator system to generate a monochromatic neutron beam with available wavelengths ranging from 1.45 Å to 2.67 Å and flux of $\sim 3 \times 10^7$ n/cm^2/s. The incident and diffracted slits are customizable to achieve desired gage volume. Scattered neutrons are collected by an array of 7 Linear Position Sensitive Detectors covering a 34° range (± 17°) out of the

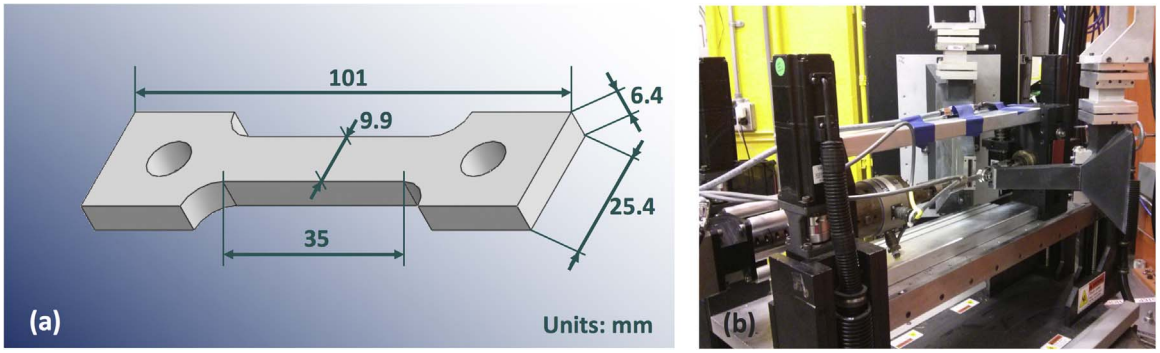

Fig. 1. (a) Sample model (b) instrument stage showing Z elevator, and load frame.

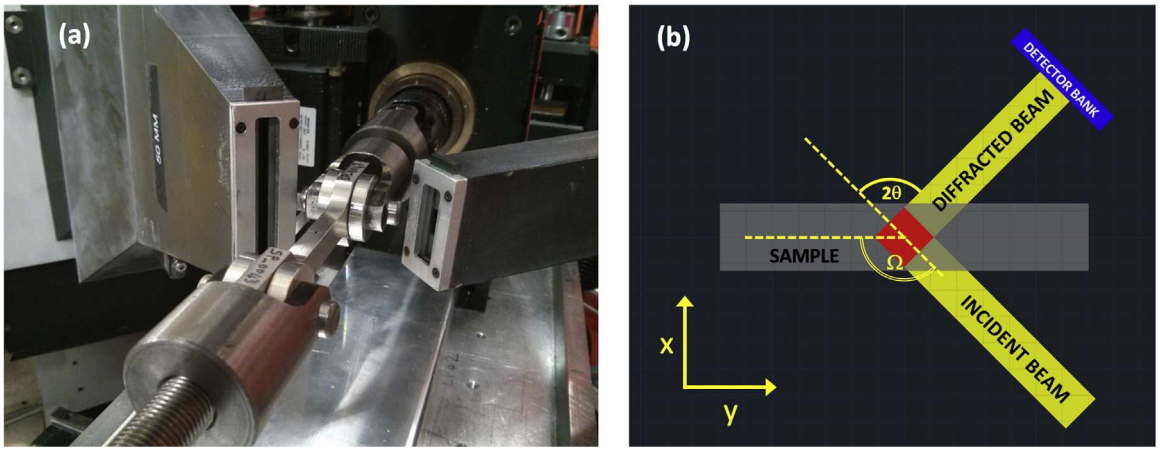

Fig. 2. (a) Schematic representation of sample, neutron beam and detector bank, and the load frame (b) detail showing the orientation of diffraction vector.

diffraction plane. The sample platform is built on a stage capable of motion in the **X** and **Y** directions as well as omega **Ω** rotation (Fig. 2(b)). Vertical **Z** motion is implemented by the integration of a custom Z stage elevator. The portable load frame was mounted horizontally on the instrument stage (Fig. 1(b)) and authors integrated its controlling hardware and software with NRSF2 to enable control of mechanical loads and automated neutron diffraction measurements from the instrument workstation.

2.4. Alignment and neutron diffraction measurements

Neutron scans in the X and Y directions were carried out using a pin mounted in the center of the stage prior to mounting the load frame. After precisely aligning the pin, its location in space was referenced using a system of three theodolites. The sample (mounted in the load frame) was marked in the center of its gage section and aligned using the reference theodolites. A refined alignment was made with neutron scans from edge to edge along the width of the sample.

The sample was in the plane of the incident and diffracted beams as shown in Fig. 2(a) and using the tunable monochromator, the $d_{(311)}$, $d_{(222)}$ and $d_{(400)}$ interplanar spacings were probed with scattering angles 2θ close to 90°. Strain resolution is higher at narrower 2θ angles; however, such angles produce an elongated, diamond-shaped gage volume which probes strains from a wider sample region. Additionally, at a narrow 2θ angles, the diffraction cone projection on the detector appears as a curved line whereas for 2θ ~ 90° the Debey-Scherrer cone becomes a vertical disk making integration of out of plane diffraction data less prone to error [21]. Table 2 summarizes settings used for each diffraction measurement to measure target *hkl*'s.

For various *hkl*'s, the stage and detector bank were rotated to Ω and 2θ values to keep the sample's axis aligned with the diffraction vector thus always measuring d-spacing changes along the direction of applied load.

Table 2
List of *hkl*'s, instrument and stage angles, and neutron beam wavelengths used.

hkl	(311)	(222)	(400)
2θ	89°	94°	90°
ω	134.5°	137°	135°
λ	1.73 Å	1.73 Å	1.45 Å

A schematic representation showing the sample, instrument axis, angles and gage volume defined by incident and diffracted slits is shown in Fig. 2(b). Authors chose data acquisition time (per data point) based on scattering intensity of the reflection of interest, and pseudo-Voigt fit to raw data was implemented to determine peak position intensity and width.

2.5. Mechanical loading

2.5.1. Elastic response

Authors subjected samples to 4 elastic load/unload cycles. During these cycles when the target stress states were reached, the deformation was halted to keep the desired stress amplitude constant for the duration of the neutron diffraction measurement; step size was ~ 5 MPa. Virgin alloy based samples were subjected to a maximum tensile stress of 200 MPa while samples exposed to 400 °C were loaded to a maximum stress of 90 MPa to ensure the maximum stress remained within elastic limits.

2.5.2. Plasticity behavior

After investigating the material's elastic response, plastic deformation was applied to the samples at a slow and constant tensile displacement rate of 8 μm/min (strain rate ~ 0.0004%); for these

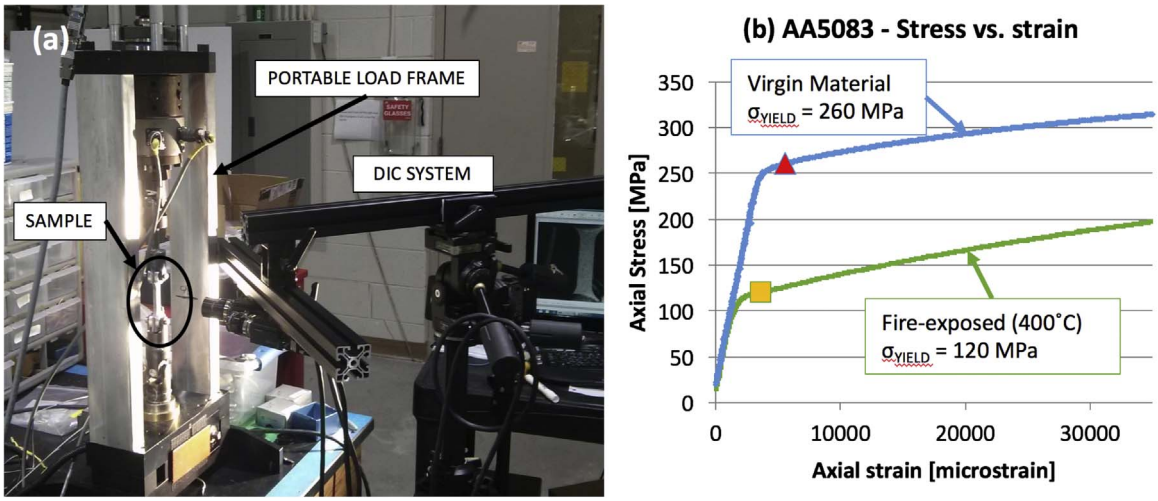

Fig. 3. (a) Experimental setup showing portable load frame and VIC-3D™ DIC system (b) stress-strain curve of virgin and fire-exposed Aluminum 5083 subjected to tension.

measurements at slow tensile rate, axial stress values varied only slightly during individual diffraction peak measurements. Samples were deformed to a target total tensile deformation ranging between 3 and 5 mm. Axial load was then brought back to seating stress and d-spacings were measured at a few points on the unloading curve.

3. Results

3.1. Macroscopic stress-strain curve

From VIC-3D™ measurements (the setup with portable load frame and DIC is shown in Fig. 3(a)), the macroscopic Young's modulus was found to be 66.9 GPa with a yield stress of 260 MPa for the virgin material. The fire-exposed sample showed a Young's modulus of 68.5 GPa and a yield stress of 120 MPa. These results are comparable with values found in literature [11]. The strength reduction is associated with coarsening of grains with recovery of dislocations, depletion of α-phase of Magnesium from the precipitation of Al_2Mg_3 β-phase. Data from DIC comparing stress-strain curves are summarized in Fig. 3(b).

3.2. Elastic load/unload cycles, step loading

From the elastic load/unload cycles, the *hkl* specific Young's Moduli are determined. An example of stress vs. lattice strain for the (222) *hkl* of virgin material is shown in Fig. 4. Obtained values are comparable to results from literature [16] and are presented in Table 3:

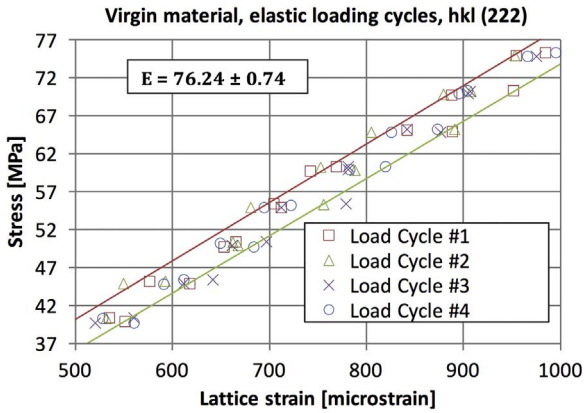

Fig. 4. Detail of stress vs. (222) lattice strain for virgin material sample.

Table 3
Tabulation of Young's Modulus values for various *hkl*'s. Units: GPa.

hkl	(311)	(222)	(400)
Virgin material	74.59 ± 1.30	76.24 ± 0.74	76.39 ± 2.37
Fire-exposed (400 °C)	72.69 ± 2.41	75.87 ± 3.11	71.93 ± 1.90

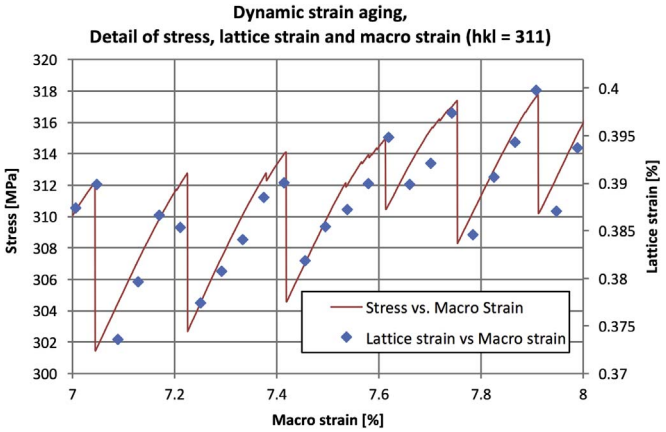

Fig. 5. A detail of the stress-strain curve with a superimposed lattice strain vs. strain curve for the same stress range.

3.3. Dynamic strain aging

During plastic deformation (at a constant rate of 9 μm/min) of virgin material samples, dynamic strain aging (DSA) was observed with the stress-strain curve showing a saw-toothed shape as seen in Fig. 5.

3.4. Continuous plastic deformation

Virgin material samples: A plot of macro strain against lattice strain (Fig. 6(a)) shows response of three *hkl*'s to applied load. D-spacings show linear behavior up to ~3500 microstrain (tensile stress = 265 MPa); plasticity onset shows a distinct slope with sharp decrease in lattice strain for a comparable macro strain. Slopes in the plastic region remain similar to each other for different *hkl*'s. Fire-exposed (400 °C) samples: for these samples, the lattice strain response (Fig. 6(b)) of the three *hkl*'s remains linear up to 1400 microstrain. At this point, the (400) lattice plane family is the first to exhibit a slope change. At approximately 1500 microstrain, strain corresponding to the (311) lattice plane family ceases to increase until macrostrain increases beyond 4500

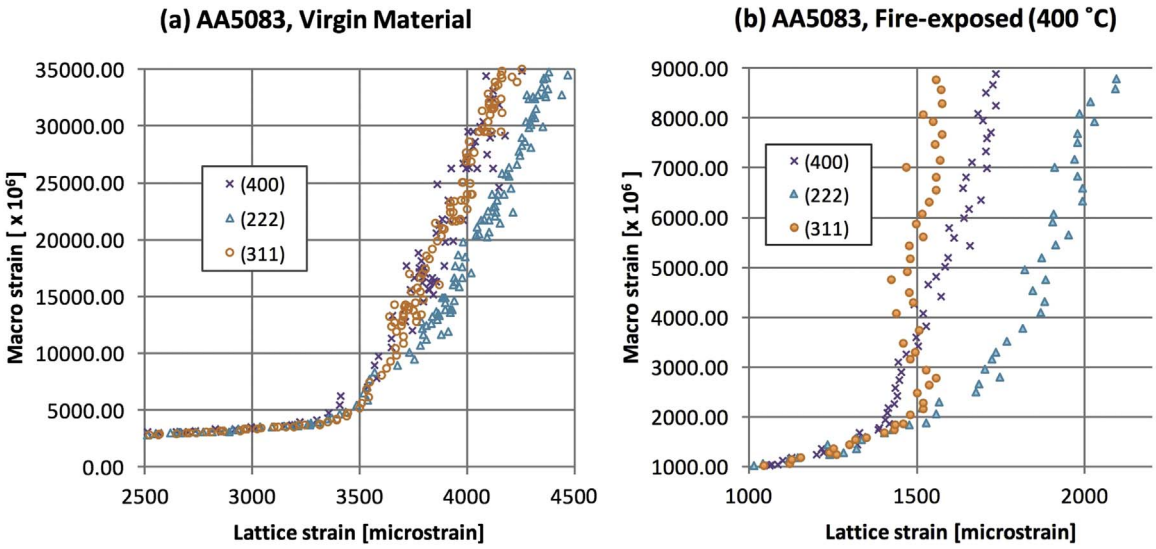

Fig. 6. A plot showing *hkl* response to engineering macro strain for (a) virgin material samples and (b) fire-exposed (400 ˚C) samples.

microstrain, when the lattice strain increases again approximately linearly. The strain corresponding to the (222) lattice planes remains linear up to ~ 1600 microstrain. The transition into the plastic regime is smoother than the ones observed for (400) and (311) planes. D-spacings $d_{(311)}$ and $d_{(222)}$ were measured during the same tension measurement by alternating detector position (and corresponding Ω angle) to measure (311) and (222) peaks.

When plotting the macroscopic stress vs. lattice strain, trends from virgin material and fire-exposed samples display a similar behavior (Fig. 7). However, strains are more uniform in the fire-exposed treated sample, and Fig. 7(b) allows a clearer understanding of the yield process. In particular, we focus on the region where the *hkl* specific strains deviate from linearity.

Scatter in the diffraction data is reduced for fire-exposed samples due to lack of serrations in the plastic region. Before yielding, a linear relation is exhibited between applied stress and lattice strain. Just above 100 MPa the (400) plane is the first to deviate from linear behavior; for an increase in stress, strain increases at a much slower rate up to ~ 120 MPa, then the slope of the curve returns close to its pre-yield value. At an axial stress of ~ 114 MPa, (311) shows no increase in lattice strain for a corresponding stress increase, and on the other hand the (222) planes show an increase in strain with no significant stress change. Shortly after, at approximately 120 MPa, both *hkl*'s return to similar strain to stress dependency. Behavior of (311) and (222) planes in samples exposed to 400 ˚C, shown in Fig. 7(b), indicates that when more compliant planes (such as the (311) and (400) planes) yield, the load bearing is shifted to other planes where slipping is yet to take place [22]. A similar behavior is observed in an in situ neutron diffraction study of interstitial-free steel [23]. A comparison of curve slopes pre and post-yield is shown in Table 4.

Peak intensity (in both fire-exposed and virgin material samples) changes for differing *hkl*'s. Fig. 8 shows the (311) and (400) planes decrease in intensity while intensity increases for the (222) reflection. After yield, as shown in Fig. 9, Full Width Half Maximum (FWHM) increases with plastic deformation for all reflections due to increase in defects and dislocations.

3.5. Electron backscatter diffraction and energy dispersive spectroscopy

EBSD maps were obtained at resolutions of 400–500 by 300–375

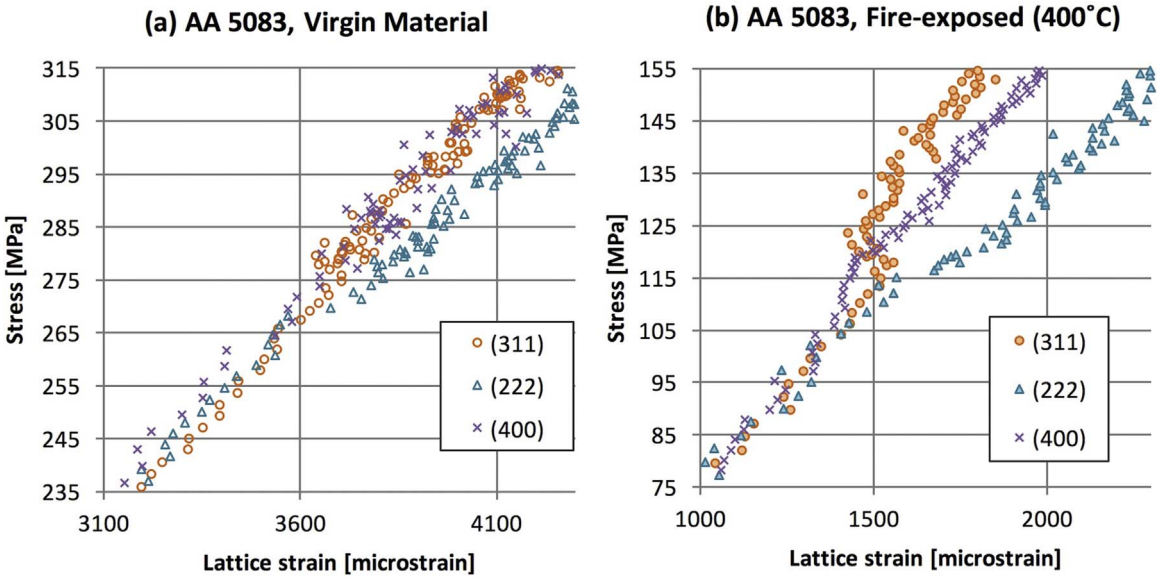

Fig. 7. Stress vs. lattice strain for (a) virgin material sample and (b) fire-exposed sample.

Table 4
Slope of stress strain curve pre-yield and post-yield. Units: GPa.

	Continuous loading	E (400)	E (222)	E (311)
Pre-yield	Virgin material	76.12	74.76	73.83
	Fire-exposed (400 °C)	77.02	70.49	75.53
Post-yield	Virgin material	51.26	57.32	64.24
	Fire-exposed (400 °C)	65.03	65.65	70.24

pixels. Beam voltage was 20 kV and exposure time ranged between 7 and 14 ms for various maps. Due to grain morphology virgin material returned a higher percentage of zero solutions. Grains were highly elongated and extended beyond the scope of the map. Imaging of the fire-exposed samples was less challenging; average grain size was found to be 15.6 μm and 42.5 μm for strained and unstrained samples respectively. EDS revealed the presence of Manganese/Iron and Silicon/Magnesium precipitate sites.

4. Discussion

4.1. Elastic load/unload cycles, step loading

For step loading, values and errors were determined from finding the average values of modulus and intercept (seating stress) plus or minus one standard deviation (SD). The continuous lines in Fig. 4, encompassing data points are obtained by using the maximum (E_{hkl} + SD, Intercept + SD) and minimum (E_{hkl} – SD, Intercept – SD) E_{hkl} and seating stress values respectively.

For both virgin and fire-exposed material, lattice specific elastic moduli are very close to each other indicating lack of elastic anisotropy for the investigated reflections [16,21]. In fire-exposed samples, a slight reduction in modulus (ranging 1–6%) is observed compared to virgin material but considering error values this decrease is practically negligible.

4.2. Dynamic strain aging

During plastic deformation of virgin material samples, DSA was observed. EBSD results, shown in Fig. 10(a) and (c), revealed an elongated grain structure for virgin material samples that transforms to an equiaxed one after fire-exposure indicating recrystallization (Fig. 10(b) and (d)). Recrystallization leads to the removal of dislocations hence the absence of DSA behavior in the stress strain curve for fire-exposed samples. A detailed look at a sub-region of the stress strain curve in Fig. 5 shows the sample displaying type C serrations which typically occur due to dislocation unlocking at low strain rates [24]. Due to rapid acquisition times for the 311 reflection, dynamic strain aging was captured, in a novel manner, by neutron diffraction during continuous axial deformation, and overlaid diffraction data closely matches macroscopic stress-strain behavior.

4.3. Continuous plastic deformation and microstructure analysis

Virgin material displays nearly isotropic behavior both during elastic and plastic deformation. The introduction of magnesium and other alloying elements gives rise to DSA and appears to make material behavior less dependent on lattice orientation during plastic deformation. Stress vs. lattice strain curves for fire-exposed treated samples show higher deviation from elastic behavior as compared to virgin material samples revealing occurrence of plastic anisotropy. Peak intensity changes after yield, shown in Fig. 8, indicate stress induced lattice rotation during slip processes [16]. Increase of FWHM for all reflections (Fig. 9) is related to growing number of defects. A steeper FWHM change is observed for the (222) reflection, suggesting that as more (222) planes align normal to the loading axis, strains become unevenly distributed. For the virgin material in this study FHWM values for each reflection are higher than the corresponding fire-exposed measured widths indicating larger Type II and III microstresses [21]. Cold worked metals are known to have a much higher dislocation density as compared to annealed material. In single crystals, dislocation are unevenly distributed with higher density close to the surface [25]. SEM imaging combined with EDS in Fig. 11, shows presence of precipitates in virgin material from rolled plate; after fire exposure Manganese/Iron precipitates grow to larger size while there is a reduction in Silicon/Magnesium sites [8].

EBSD has shown that microstructure of virgin material samples consists of flat, highly elongated grains. Considering the microstructure of these samples, a high number of dislocations is expected at grain

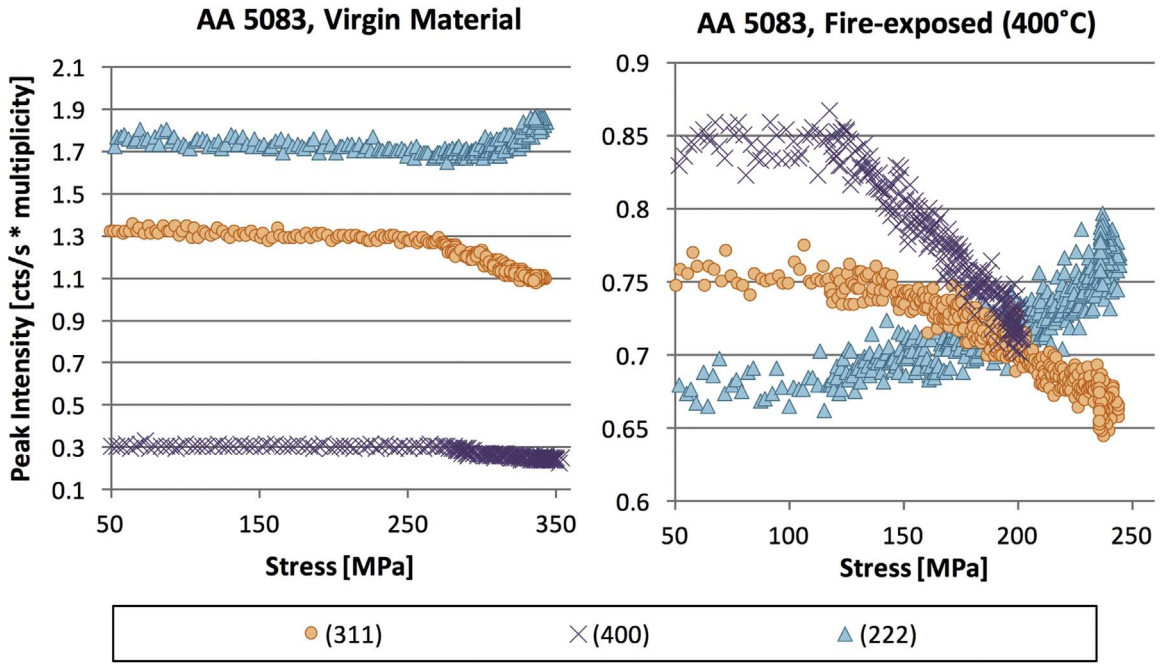

Fig. 8. A plot of peak intensity variation with applied axial stress.

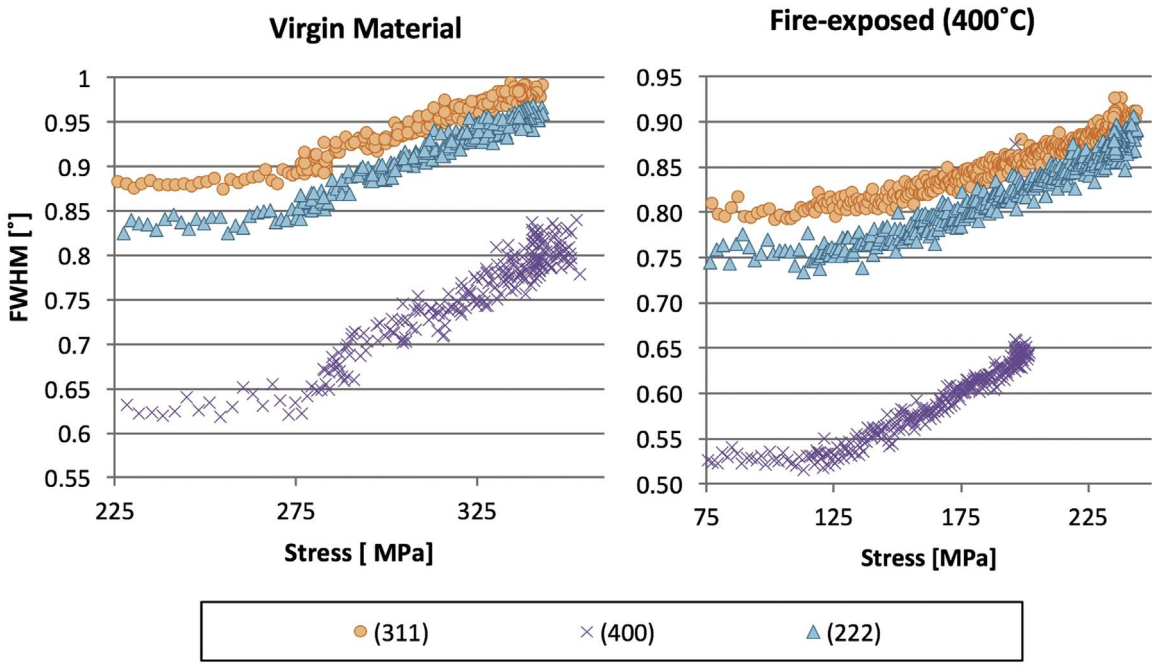

Fig. 9. Plot of FWHM variation with applied stress.

boundaries. These dislocations may account for the inability of lattice planes to rotate with increasing stress. Fire-exposed samples, with a lower number of dislocation and a more equiaxed grain structure, are free to allow rotation of lattice planes thus leading to an increased deviation from linear elastic behavior after material yield. A comparison of unstrained (Fig. 10(a) and (b)) and strained materials (Fig. 10(c) and (d)) reveals strain-induced grain refinement. For virgin material grains appear to align further with loading direction and become thinner in the normal direction while grains in fire-exposed samples reduce significantly in size.

Pole figures obtained from EBSD data are shown in Fig. 12. Fig. 12(a) displays initial texture due to plate rolling in virgin

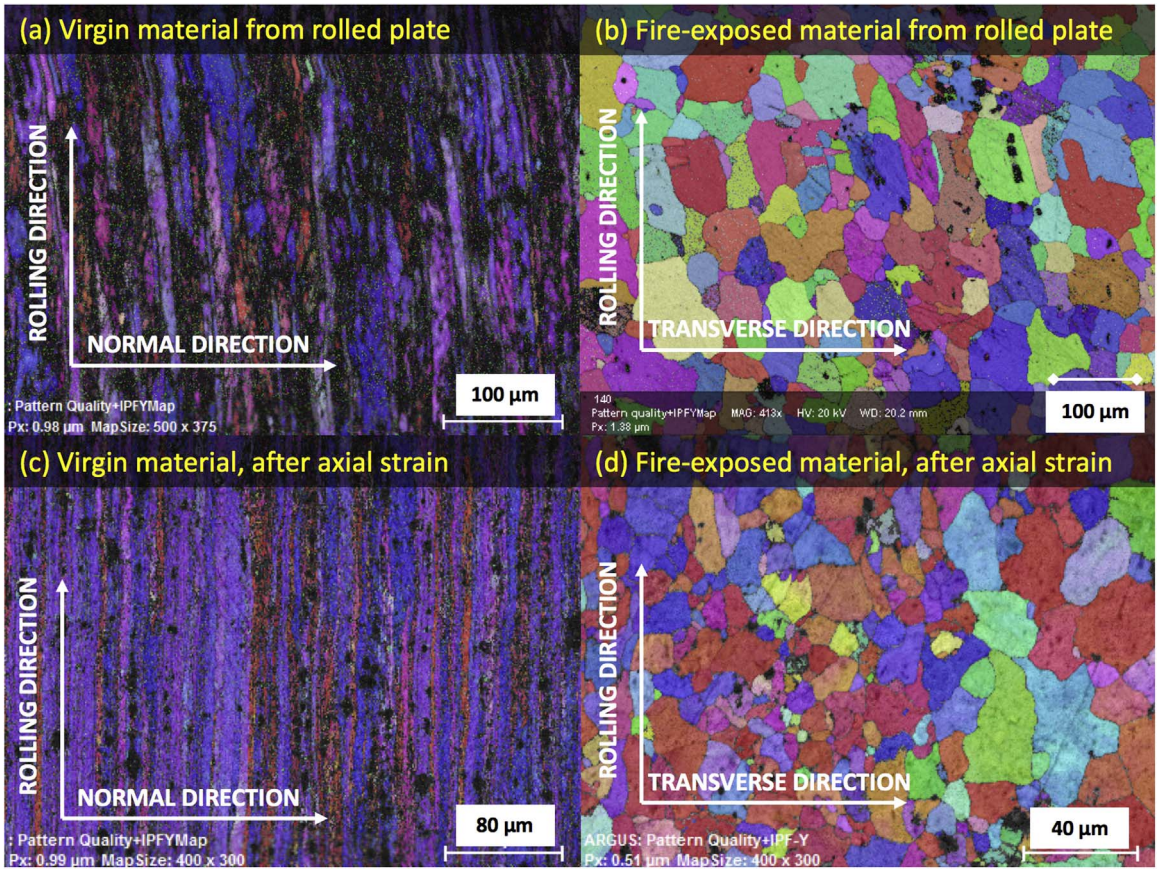

Fig. 10. Microstructure from (a) unstrained virgin material sample, (b) unstrained fire-exposed sample, (c) strained virgin material sample, and (d) strained fire-exposed sample.

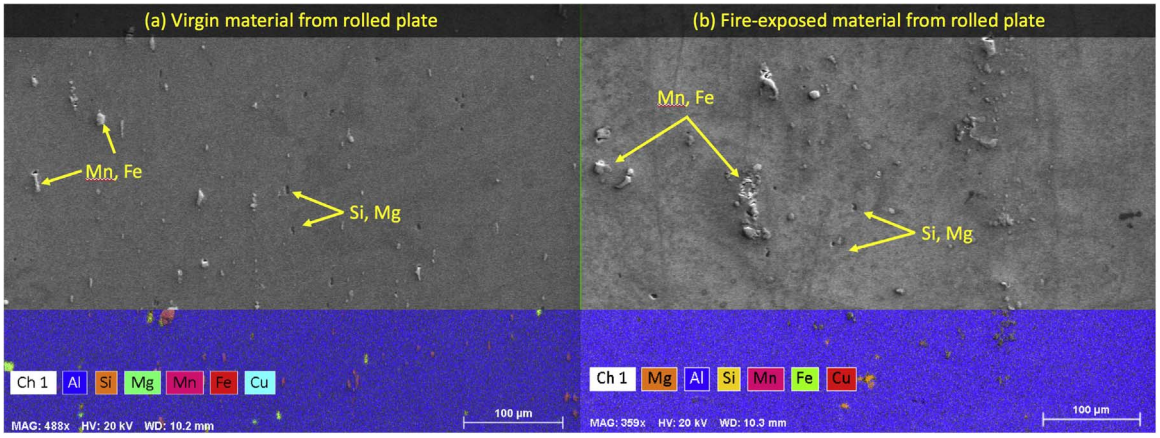

Fig. 11. SEM/EDS images of unstrained virgin material (a) and fire-exposed material (b).

unstrained material; strained virgin material presents a more accentuated texture in Fig. 12(c) but overall, grains maintain a similar orientation. On the other hand, subsequent to fire exposure, texture is considerably relieved as shown in Fig. 12(b) and a new preferred orientation arises after axial strain Fig. 12(d). The fire-exposed {111} pole figures are consistent with data reported for typical texture of recrystallized rolled aluminum [25]. Texture studies on AA5083 subjected to uniaxial tension at various temperatures report similar textures for tensile tests carried out at 535 °C and a strain rate of 10^{-1} s^{-1} [8].

5. Conclusions

In-situ neutron diffraction to obtain lattice specific strains and moduli for the 5083 aluminum alloy was carried out in tension. Experiments indicate a degradation in yield stress from 260 MPa to 120 MPa due to fire exposure and subsequent water quenching. Using neutron diffraction and portable load frame, $d_{(311)}$, $d_{(222)}$ and $d_{(400)}$

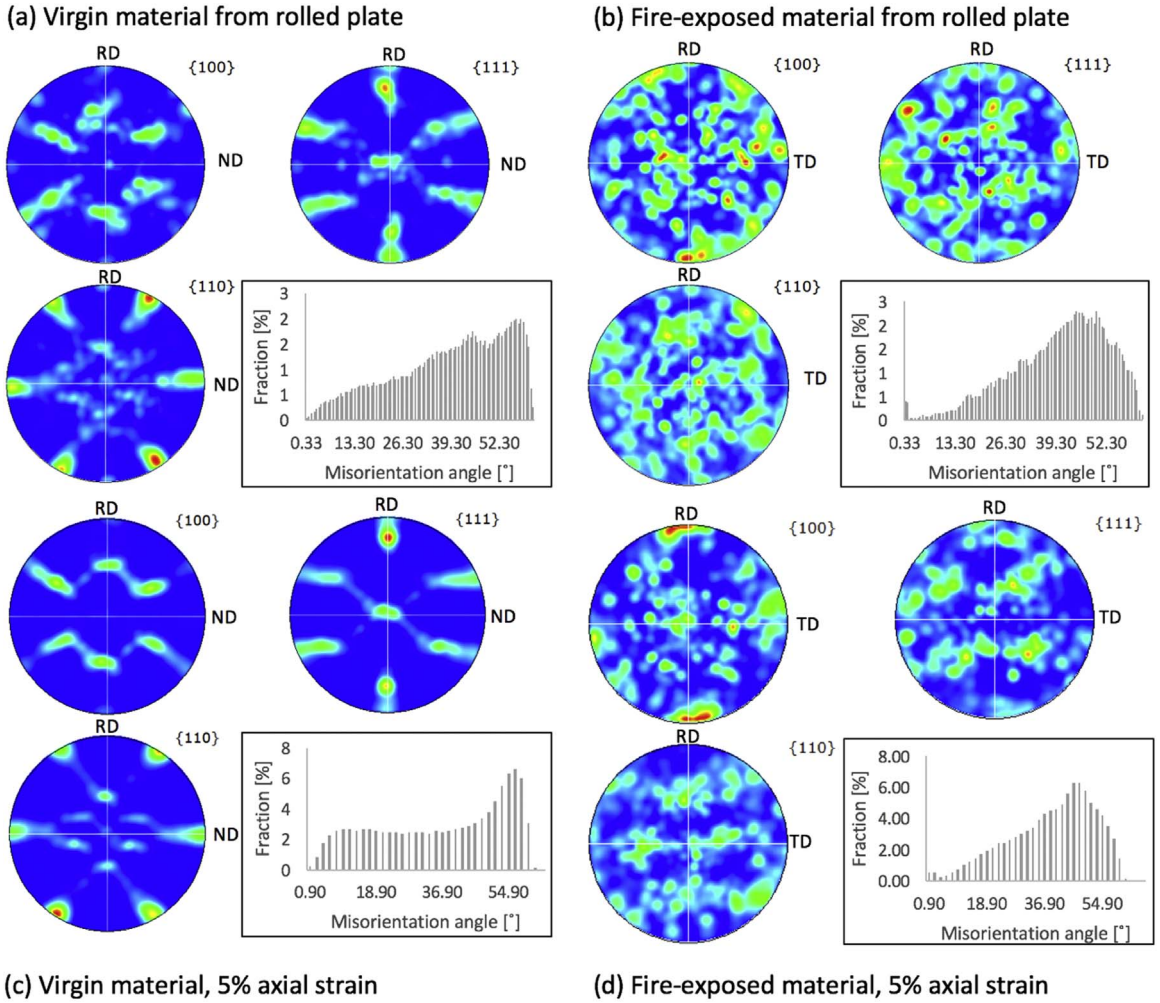

Fig. 12. Pole figures and misorientation profiles of (a) unstrained virgin material sample, (b) unstrained fire-exposed sample, (c) virgin material sample subjected to axial strain, and (d) fire-exposed sample subjected to axial strain.

interplanar spacings were probed in detail for elastic (pre-yield) and plastic (post-yield) loading conditions. Dynamic strain aging, exhibited by the virgin marine aluminum alloy and captured for the (311) reflection during in situ measurements, disappeared after subjecting to fire damage with samples exposed to 400 °C. High frequency data for stress vs. lattice strain curves showed detailed transition from elastic to plastic regions of the stress-strain curve. In fire-exposed specimen the (400) plane was the first to deviate from linear behavior. Observed plastic anisotropy (broadening in stress strain curves) during plasticity evolution is likely due to fewer dislocations and coarsening of strengthening magnesium phases allowing lattice rotations and strain redistribution. Microstructure analysis shows fire-exposure affects grain morphology creating a more equiaxed grain structure and a randomized texture while mechanical loading and plastic deformation lead to a refined grain structure and a preferred texture. The measurements reported in this paper provide a better understanding of the failure mechanisms in the AA5083 alloy, allow comparison with other alloys such as the AA6061 alloy, and are of interest for marine and naval applications. Subsequent finite element modeling will provide a framework to predict mechanical property degradation and plastic anisotropy in polycrystalline alloys.

Funding sources

Professor Penumadu would like to acknowledge the support of the United States Office of Naval Research through Grant N000141110875 with Program Managers Dr. William Mullins and Dr. Steve Turner.

Acknowledgments

The authors acknowledge the assistance of Mr. P. Cornwell and Dr. L. Kolbus related to the setup of load frame and diffraction experiments at NRSF2. A portion of this research related to neutron diffraction measurements at the Oak Ridge National Laboratory High Flux Isotope Reactor was sponsored by the Scientific User Facilities Division, Office of Basic Energy Sciences, United States Department of Energy. Authors also gratefully acknowledge the contributions of collaborators through the larger ONR Fire and Structures Research Program, specifically Drs. Patrick Summers, Brian Lattimer, and Professor Scott Case, at Virginia Tech in Blacksburge, VA, and Professor Adrian Mouritz at the Royal Melbourne Institute of Technology (RMIT) in Australia.

References

[1] J. Ye, L. Ajdelsztajn, J.M. Schoenung, Bulk nanocrystalline aluminum 5083 alloy fabricated by a novel technique: cryomilling and spark plasma sintering, Metall. Mater. Trans. A 37 (2006) 2569–2579.
[2] R.A. Sielski, Research needs in aluminum structure*, Ships Offshore Struct. 3 (2008) 57–65.
[3] M. Scott, M. Gittos, Tensile and toughness properties of arc-welded 5083 and 6082 aluminum alloys, Weld. J. 62 (1983) 243s–252s.
[4] M. Dvornak, R. Frost, D. Olson, The weldability and grain refinement of AI-2.2Li-2.7Cu,", Weld. J. 68 (1988).
[5] L.E. Svensson, L. Karlsson, H. Larsson, B. Karlsson, M. Fazzini, J. Karlsson, Microstructure and mechanical properties of friction stir welded aluminium alloys with special reference to AA 5083 and AA 6082, Sci. Technol. Weld. Join. 5 (2013) 285–296.
[6] Ø. Ryen, B. Holmedal, O. Nijs, E. Nes, E. Sjölander, H.-E. Ekström, Strengthening mechanisms in solid solution aluminum alloys, Metall. Mater. Trans. A 37 (2006) 1999–2006.
[7] Properties and selection: nonferrous alloys and special-purpose materials, in: Metals Handbook, vol. 2, 10th ed., ASM International, 1990.
[8] I.N.A. Oguocha, O.J. Adigun, S. Yannacopoulos, Effect of sensitization heat treatment on properties of Al–Mg alloy AA5083-H116, J. Mater. Sci. 43 (2008) 4208–4214.
[9] S. Agarwal, P.E. Krajewski, C.L. Briant, Dynamic recrystallization of AA5083 at 450 °C: the effects of strain rate and particle size, Metall. Mater. Trans. A 39 (2008) 1277–1289.
[10] R.L. Holtz, P.S. Pao, R.A. Bayles, T.M. Longazel, R. Goswami, Corrosion-fatigue behavior of aluminum alloy 5083-H131 sensitized at 448 K (175 °C), Metall. Mater. Trans. A 43 (2011) 2839–2849.
[11] P.T. Summers, S.W. Case, B.Y. Lattimer, Residual mechanical properties of aluminum alloys AA5083-H116 and AA6061-T651 after fire, Eng. Struct. 76 (2014) 49–61.
[12] M.R. Daymond, H.G. Priesmeyer, Elastoplastic deformation of ferritic steel and cementite studied by neutron diffraction and self-consistent modelling, Acta Mater. 50 (2002) 1613–1626.
[13] M.A. Gharghouri, G.C. Weatherly, J.D. Embury, J. Root, "Study of the mechanical properties of Mg-7.7 at% Al byin-situneutron diffraction, Philos. Mag. A 79 (1999) 1671–1695.
[14] J.W.L. Pang, T.M. Holden, T.E. Mason, In situ generation of intergranular strains in an Al7050 alloy, Acta Mater. 46 (1998) 1503–1518.
[15] S.R. Agnew, C.N. Tomé, D.W. Brown, T.M. Holden, S.C. Vogel, Study of slip mechanisms in a magnesium alloy by neutron diffraction and modeling, Scr. Mater. 48 (2003) 1003–1008.
[16] B. Clausen, M.A.M. Bourke, Lattice plane response during tensile loading of an aluminum 2% magnesium alloy, Metall. Mater. Trans. A 32 (2001) 691–694.
[17] R. Ma, T.J. Truster, S.B. Puplampu, D. Penumadu, Investigating mechanical degradation due to fire exposure of aluminum alloy 5083 using crystal plasticity finite element method, Int. J. Solids Struct. (2017).
[18] R. Woracek, J.R. Bunn, D. Penumadu, C.R. Hubbard, Method to determine *hkl* strains and shear moduli under torsion using neutron diffraction, Appl. Phys. Lett. 100 (2012) 191904.
[19] R. Woracek, D. Penumadu, N. Kardjilov, A. Hilger, M. Strobl, R.C. Wimpory, et al., Neutron Bragg-edge-imaging for strain mapping under in situ tensile loading,", J. Appl. Phys. 109 (2011) 093506.
[20] VIC-3D, Correlated Solutions Incorporated, 〈http://www.correlatedsolutions.com/〉.
[21] M.T. Hutchings, P.J. Withers, T.M. Holden, T. Lorentzen, Introduction to the Characterization of Residual Stress by Neutron Diffraction, CRC press, 2005.
[22] B. Clausen, T. Lorentzen, M.A.M. Bourke, M.R. Daymond, Lattice strain evolution during uniaxial tensile loading of stainless steel, Mater. Sci. Eng.: A 259 (1999) 17–24.
[23] Y. Tomota, P. Lukas, S. Harjo, J.H. Park, N. Tsuchida, D. Neov, In situ neutron diffraction study of IF and ultra low carbon steels upon tensile deformation, Acta Mater. 51 (2003) 819–830.
[24] P. Rodriguez, Serrated plastic flow, Bull. Mater. Sci. 6 (1984) 653–663.
[25] G. Dieter, Mechanical Metallurgy, 3rd ed, McGraw Hill Education, India, 2013.